ULTRASOUND NEWS

July 2026

Early ultrasound markers for predicting the transition from acute kidney injury to chronic kidney disease and treatment response in a murine model

ULTRA
SONO
GRAPHY

ORIGINAL ARTICLE

Min Hoan Moon[1,2*], Jeonghwan Lee[3,4*], Chang Kyu Sung[1,2], Jung Pyo Lee[3,4], Myoung Seok Lee[1]

[1]Department of Radiology, Seoul Metropolitan Government Seoul National University Boramae Medical Center, Seoul; [2]Department of Radiology, Seoul National University College of Medicine, Seoul; [3]Department of Internal Medicine, Seoul Metropolitan Government Seoul National University Boramae Medical Center, Seoul; [4]Department of Internal Medicine, Seoul National University Hospital, Seoul, Korea

https://doi.org/10.14366/usg.26139
eISSN: 2288-5943
Ultrasonography 2026;45:359-368

Purpose: This study evaluated the feasibility of ultrasound (US) parameters for predicting the transition from acute kidney injury (AKI) to chronic kidney disease (CKD) and assessing the therapeutic response to 17-DMAG, a fibrosis-mitigating agent, in a murine unilateral ischemia–reperfusion injury (UIRI) model.

Methods: Male C57BL/6 mice were assigned to sham (n=16) or UIRI (n=24) groups, with half of the UIRI mice receiving 17-DMAG (20 mg/kg intraperitoneally, three times weekly). Serial US examinations were performed on postoperative days (PODs) 3 and 8 to evaluate morphological parameters (kidney size and parenchymal thickness [PT]), vascular parameters (resistive index [RI] and vascular index [VI] derived from microvascular imaging [MVI]), and tissue stiffness assessed by shear-wave speed (SWS). Pathologic fibrosis was defined as a Sirius red–positive area >4%. Diagnostic performance was evaluated using receiver operating characteristic (ROC) curve analysis.

Results: At the early stage (POD 3), vascular parameters (VI and RI) demonstrated high diagnostic performance for predicting fibrosis progression (area under the receiver operating characteristic curve, 0.948 and 0.890, respectively), with VI serving as the only significant predictor of early treatment response to 17-DMAG. At POD 8, all parameters showed significant diagnostic performance for predicting fibrosis progression. However, for treatment response, only kidney size, PT, and RI demonstrated significant ROC performance, whereas VI and SWS did not reach statistical significance. These findings reflect the temporal transition from early functional microvascular compromise to established structural remodeling and parenchymal atrophy.

Conclusion: RI and VI are promising noninvasive surrogate markers for predicting the AKI-to-CKD transition, and VI may be useful for assessing early responses to 17-DMAG treatment. Whereas conventional US parameters identify late-stage structural remodeling, MVI provides a critical diagnostic window during the acute phase by detecting early microvascular compromise. These findings highlight the potential utility of MVI for real-time monitoring of AKI progression and anti-fibrotic treatment responses in clinical practice.

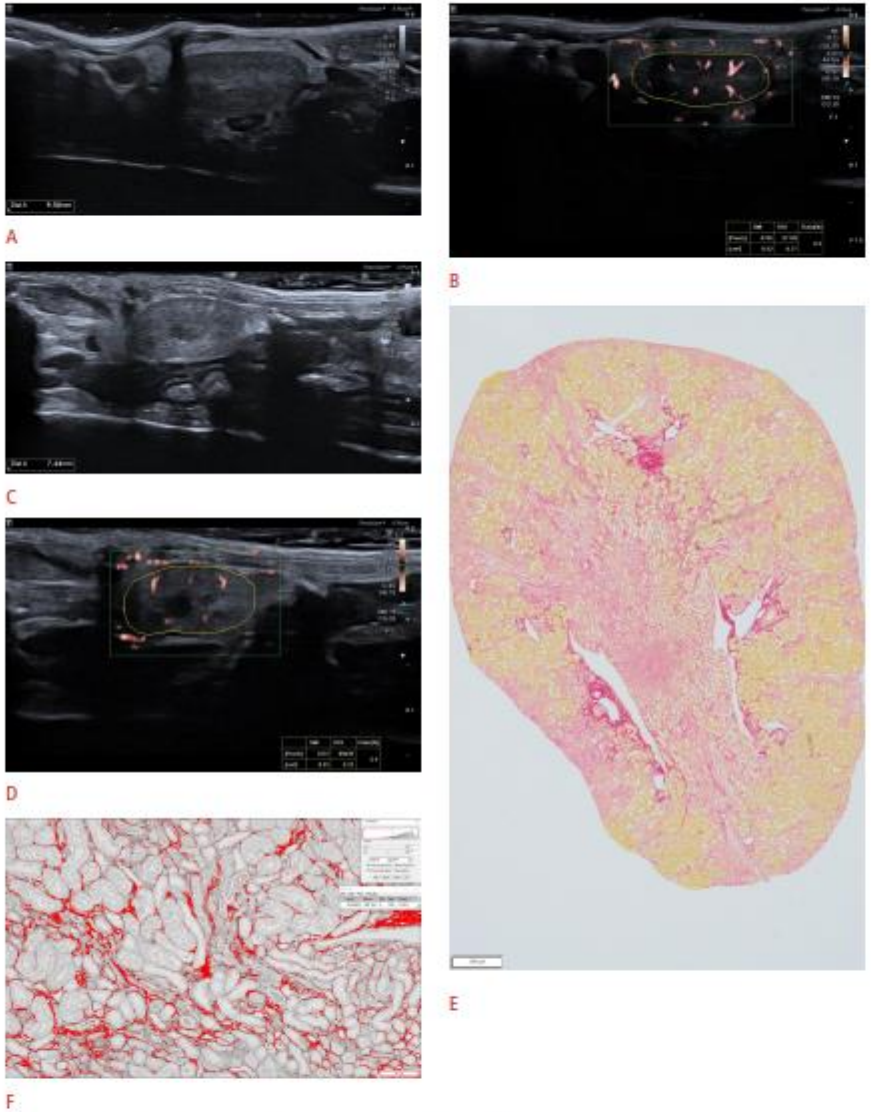

Fig. 1. Ultrasound images of a mouse kidney after unilateral ischemia–reperfusion injury.

A–D. B-mode and microvascular images of a mouse kidney were obtained on postoperative day (POD) 3 and POD 8 after unilateral ischemia–reperfusion injury. On the POD 3 B-mode image, the layered structure of the injured kidney is relatively preserved (A), with diminished flow signals on microvascular imaging (B). On POD 8, the renal parenchymal echotexture becomes heterogeneous, with loss of the layered structure (C). On microvascular imaging, flow signals are further decreased (D). E. Sirius red staining shows multifocal structural distortion with red-stained fibrosis. F. Representative fibrosis quantification image from the same Sirius red–stained specimen shown in (E) (×200), analyzed using ImageJ software. The fibrosis quantification result shows a %Area value of 10.28%, as displayed in the Results windows. Scale bars=200 μm (E), 50 μm (F). ROI, region of interest; SMI, superb microvascular imaging; %Area, Sirius red–positive area relative to the total tissue specimen area.

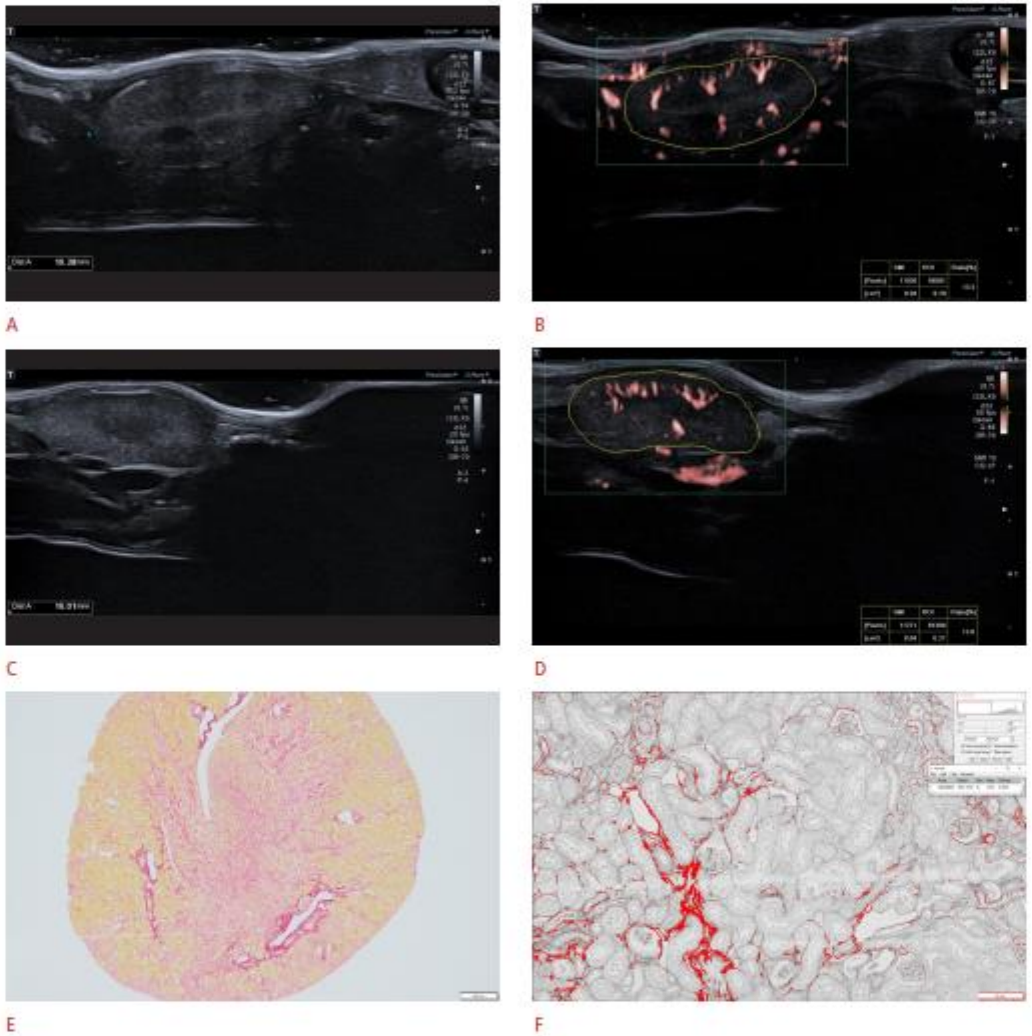

Fig. 2. Ultrasound images of a mouse kidney after unilateral ischemia–reperfusion injury with 17-DMAG treatment.

A–D. B-mode and microvascular images of a mouse kidney were obtained on postoperative day (POD) 3 and POD 8 after unilateral ischemia–reperfusion injury with 17-DMAG treatment. The layered structure of the renal parenchyma is relatively preserved on the POD 3 B-mode image (A). Flow signals are more evident than in the untreated kidney on microvascular imaging (B). On POD 8, kidney size is preserved on B-mode imaging during 17-DMAG treatment (C), without a marked decrease in flow signals on microvascular imaging (D). E. Sirius red staining shows less structural distortion and fibrosis than in the untreated kidney. F. Representative fibrosis quantification image from the same Sirius red–stained specimen shown in (E) (×200), analyzed using ImageJ software. The fibrosis quantification result shows a %Area value of 3.51%, as displayed in the Results windows. Scale bars=200 μm (E), 50 μm (F). ROI, region of interest; SMI, superb microvascular imaging; %Area, Sirius red–positive area relative to the total tissue specimen area.

Artificial Intelligence-Assisted Wireless Handheld Ultrasound for Screening Developmental Dysplasia of the Hip in Infants

Dandan Zhang, MM, Simiao Tao, MSc Student, Ping Chen, MD, Jiangtao Wang, ME, Yu Yang, MM, Xiuxiu Zhang, MM, Tieqiang Wang, BM, Hailin Pan, PhD, Jiong Chen, MM, Baoying Ye, MD

Objectives—Ultrasonography is increasingly the preferred method for infant hip screening to enable timely diagnosis and treatment of developmental dysplasia of the hip (DDH). However, its reliance on experienced specialists and bulky equipment limits its application in routine screening, particularly in resource-limited and remote settings. We aimed to develop an artificial intelligence wireless handheld ultrasound hip diagnostic system (AI-HUDs) for accurate and robust DDH diagnosis.

Methods—An AI-HUDs was developed to automatically identify and analyze 6 key anatomical landmarks in static and dynamic hip ultrasound images, employing the Graf method to measure α and β angles. The dataset comprised 1192 ultrasound images and 498 dynamic videos. The YOLOv8 model was trained and tested to construct AI-HUDs. Evaluation focused on the consistency between AI-HUDs' automatic angle measurements and manual measurements by experts using traditional ultrasound equipment. Additionally, 104 hip ultrasound videos from 52 infants were acquired by a resident physician using AI-HUDs, while corresponding static images were manually measured by ultrasound experts to assess agreement between novice-operated AI-HUDs and expert manual assessment.

Conclusions

Our study demonstrates the potential of AI-HUDs to provide an effective, efficient, and feasible automated method of measuring hip angles and performing Graf classification. It demonstrates significant potential for DDH diagnosis in primary and remote healthcare settings lacking specialized personnel and equipment.

Received October 2, 2025, from the Department of Ultrasonography, The International Peace Maternity and Child Health Hospital, School of Medicine, Shanghai Jiao Tong University, Shanghai, China (D.Z., P.C., Y.Y., X.Z., T.W., J.C., B.Y.); The Software Engineering Institute, East China Normal University, Shanghai, China (S.T., J.W., H.P.); Shanghai Key Laboratory of Embryo Original Diseases, Shanghai, China (B.Y.); and Shanghai Municipal Key Clinical Specialty, Shanghai, China (B.Y.). Manuscript accepted for publication May 19, 2026.

Dandan Zhang and Simiao Tao contributed equally to this work.

All authors are grateful to all the participating members who took part in this study, including interviewers, nurses, computer technicians, and volunteers. The authors declare no conflict of interest. This research did not receive any specific grant from funding agencies in the public, commercial, or not-for-profit sectors.

Address correspondence to Baoying Ye, No. 910, Hengshan Road, Xuhui District, Shanghai, China.

E-mail: eyby99@126.com

Hailin Pan, The Software Engineering Institute, East China Normal University, Shanghai, China.

Figure 1. Illustration of the line definitions following Graf's method and keypoint labeling. **A**, Measurement lines and α, β angles. L1: base line; L2: bony roof line; L3: cartilage roof line. **B**, Six keypoints determined based on the anatomical structures. Bony roof points (orange dots) mean L1; bony rim point and lower limb point (green dots) mean L2; bony rim point and center of labrum (yellow dots) mean L3. Two points determined a straight line. Six keypoints extracted from 3 lines.

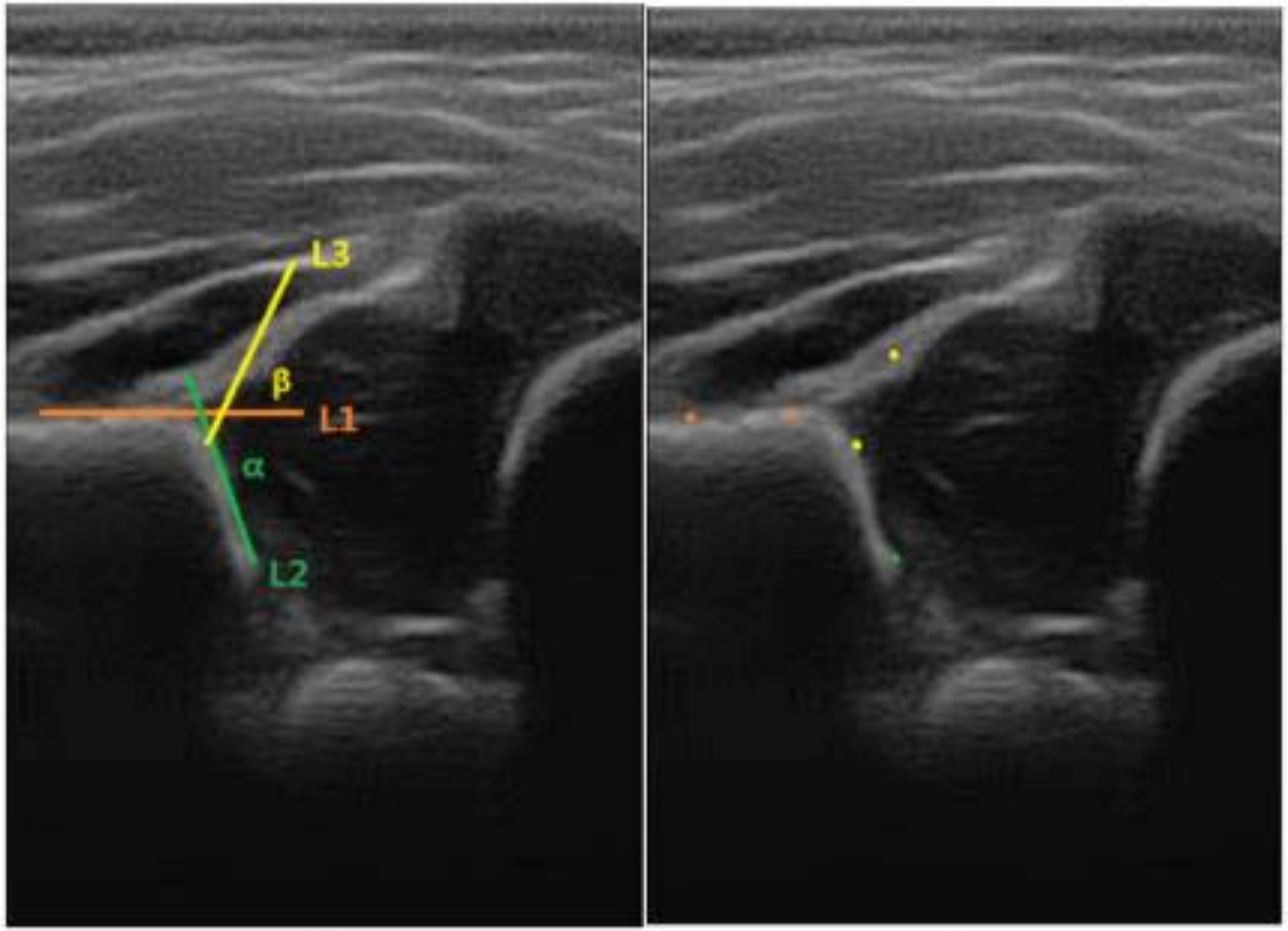

A B

Figure 2. Flow chart showing the process of selecting data.

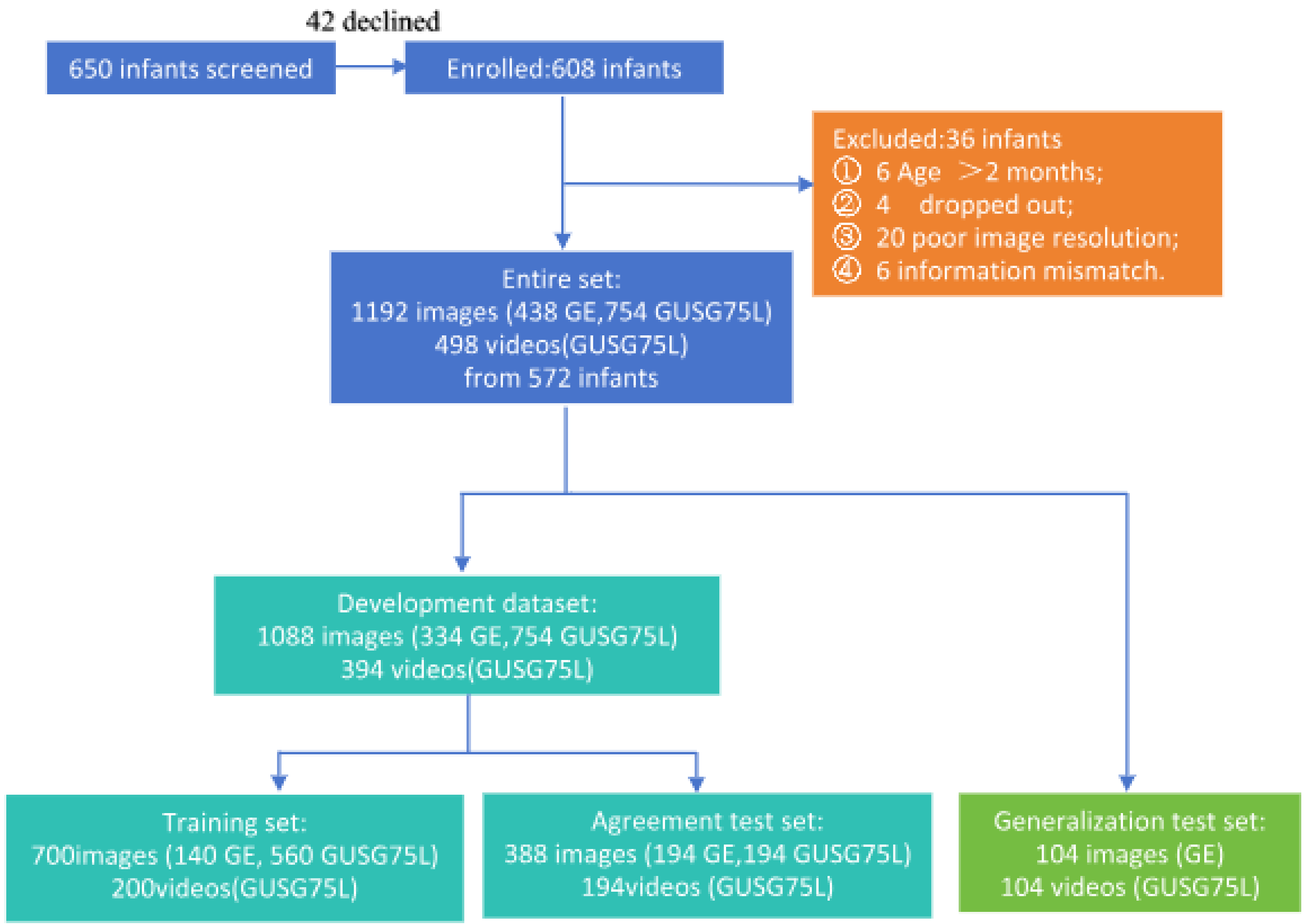

Figure 5. Process of model training and system development.

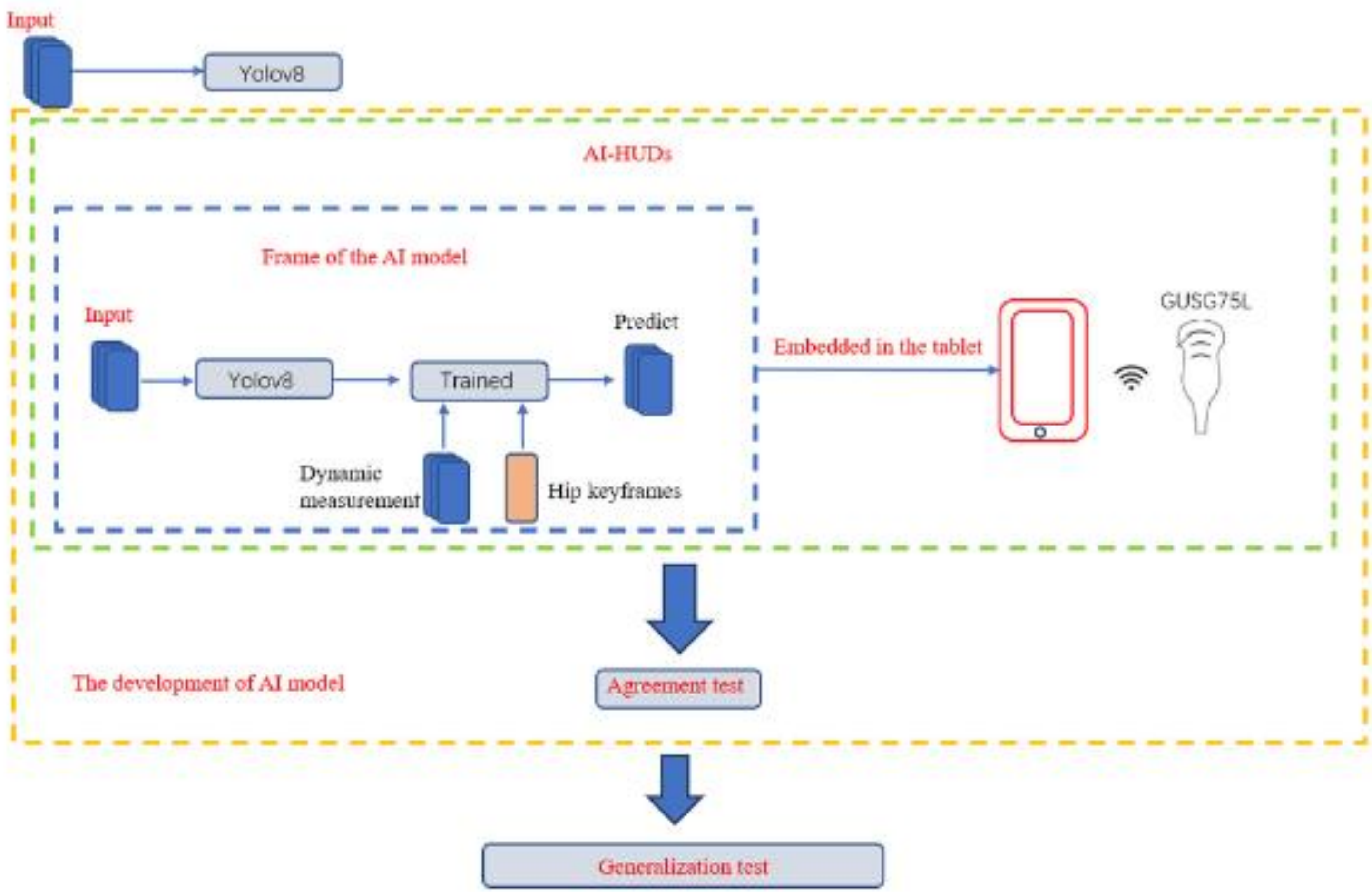

Table 1. Comparison of Angle Measurements Between Senior Sonographers and AI-HUDs in Static Mode.

Group ($n = 388$)	Mean ± SD: Senior Sonographers	Mean ± SD: AI-HUDs (Static Mode)	Difference	MAE ± SD	ICC (95%CI)	Agreement
α	67.73 ± 2.36	67.48 ± 2.22	0.25 ± 1.38	1.05 ± 0.92	0.82 (0.77 ~ 0.86)	Good (>0.7)
β	59.09 ± 2.89	58.50 ± 2.07	0.58 ± 2.14	1.65 ± 1.48	0.64 (0.55 ~ 0.71)	Moderate (0.5 ~ 0.7)

Accuracy of Key Sonographic Markers for Juxta-Articular Fractures

A Prospective Study Using Explainable Machine Learning

Xiaofang Fu, MM, Lirong Liu, PhD, Hao Sun, MM, Changqin Sun, MM, Qinhan Yang, ME, Mengjie Dou, MM, Duo Shi, MM, Junpu Hu, MM, Zhiming He, BM, Guangquan Zhou, PhD, Shiyu Jin, MM, Faqin Lv, MD

Objectives—To systematically evaluate sonographic features of long bone juxta-articular fractures and identify key diagnostic predictors using machine learning-based feature selection.

Methods—This prospective single-center diagnostic accuracy study enrolled 121 patients with clinically suspected juxta-articular fractures. Ten predefined sonographic features were assessed, with computed tomography (CT) serving as the reference standard. Key features were identified using shapley additive explanations (SHAP), and the 3 top-ranked features were used to construct a decision tree–based sonographic triad model, hereafter referred to as the sonographic triad model. This model generated a final binary ultrasound diagnosis for each suspected fracture site. Agreement between the final binary ultrasound diagnosis and CT was quantified using Cohen's κ with 95% confidence intervals (CIs). Inter-observer and intra-observer agreement was evaluated using blinded dual-reader review across the cohort. Diagnostic performance was quantified by sensitivity, specificity, predictive values, and the area under the receiver operating characteristic curve (AUC).

Conclusion

This prospective study demonstrates that the sonographic triad model, incorporating subperiosteal hematoma, arc-shaped fracture end, and heterogeneous intra-articular effusion, provides a highly accurate screening and triage approach for suspected juxta-articular long bone fractures, with high concordance with CT. This focused, rapid and radiation-free approach is particularly valuable for radiation-sensitive populations are inconclusive, while further imaging should be considered when clinical suspicion persists. Further multicenter studies are warranted to validate these findings and to assess the learning curve and diagnostic performance of the sonographic triad model among broader POCUS users.

Supplemental material online at jultrasoundmed.org

Received November 11, 2025, from the Department of Ultrasound Medicine, The Eighth People's Hospital of Shanghai, Shanghai, China (X.F.); Department of Ultrasonography, The Third Medical Center of Chinese PLA General Hospital, Beijing, China (L.L., H.S., M.D., J.H., S.J., F.L.); Department of Ultrasound, Tianjin Rehabilitation and Convalescent Center of Chinese People's Liberation Army, Tianjin, China (H.S.); Department of Ultrasound, Shanghai YangZhi Rehabilitation Hospital (Shanghai Sunshine Rehabilitation Center), School of Medicine, Tongji University, Shanghai, China (C.S.); School of Biological Science and Medical Engineering, Southeast University, Nanjing, China (Q.Y., G.Z.); Department of Ultrasound Medicine, Peking University

Figure 2. Sonographic features of juxta-articular long bone fractures. **A**, Linear cortical separation (thick arrow); **B**, step-off sign (thick arrow); **C**, angulation (thick arrow) and peri-fracture hematoma (*); **D**, cortical overlapping (thick arrow), "arc-shaped fracture end" (△) and peri-fracture hematoma (*); **E**,**F**, cortical fragmentation sign (thick arrow) accompanied by subperiosteal hematoma (thin arrow); subcutaneous soft tissue edema of varying degrees is observed in (**A**–**F**).

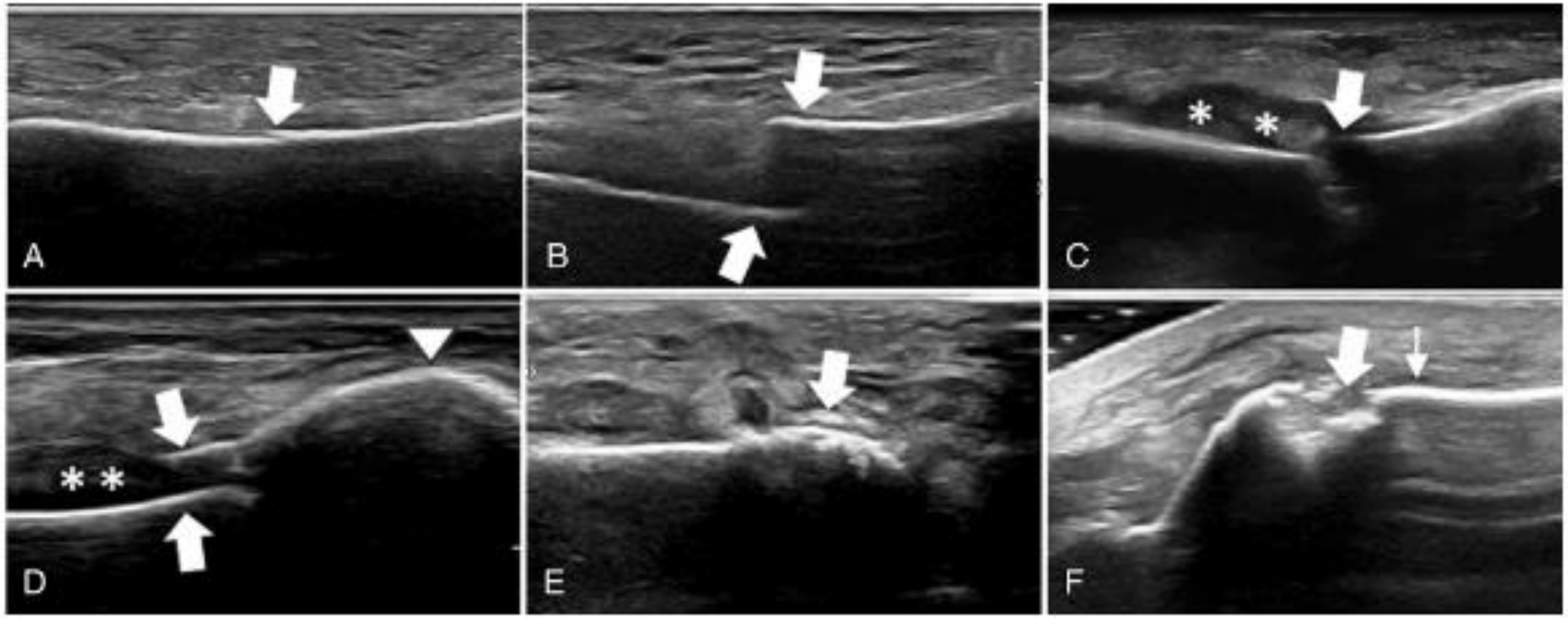

Figure 3. Comparison of 2D ultrasound, CT, and x-ray images in juxta-articular fractures. **A,B**, 2D ultrasound images showing "arc-shaped fracture ends" in the distal tibia and fibula (arrows). **C,D**, Corresponding CT coronal and sagittal images (arrows), respectively. **E**, 2D ultrasound image showing fracture-associated soft tissue edema (arrow), characterized by soft tissue thickening, increased echogenicity, slit-like hypoechogenicity, and blurred boundaries between layers. **F,G**, Corresponding x-ray images (anteroposterior and lateral views, arrows), showing local thickening of subcutaneous soft tissue with slightly higher density than surrounding normal soft tissue.

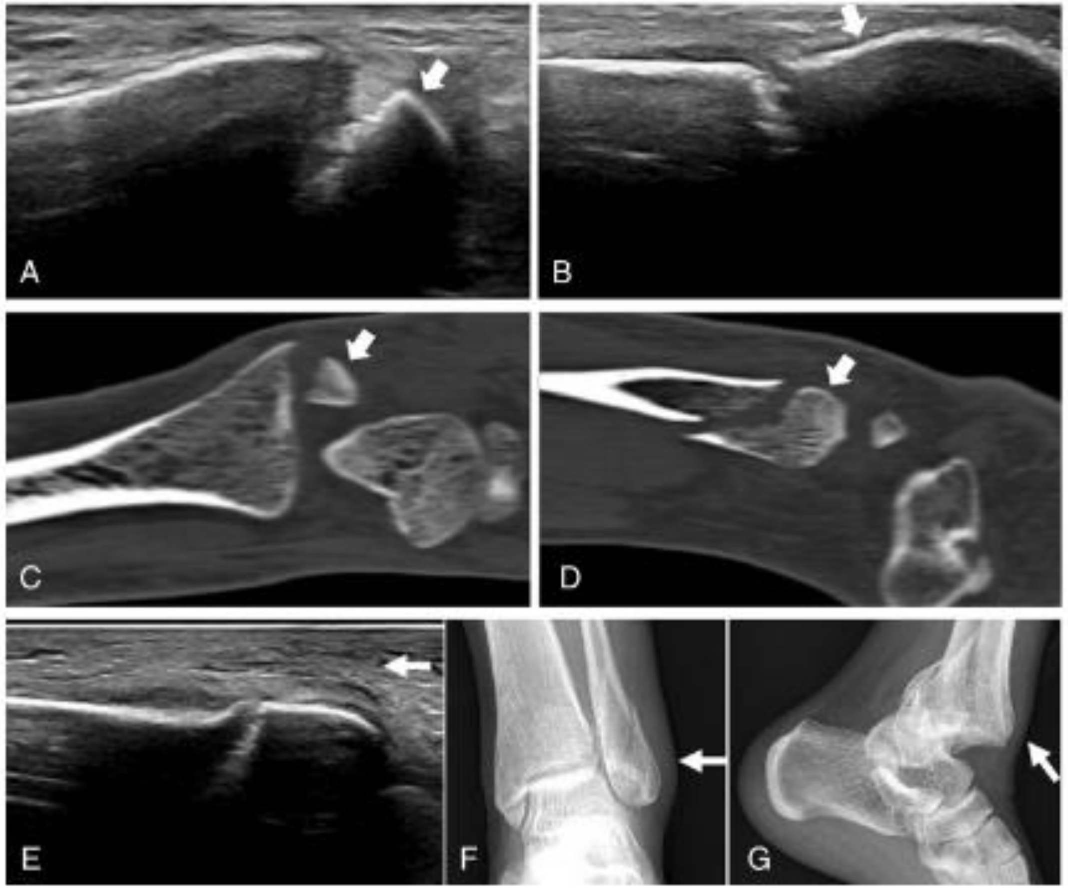

Figure 4. Ultrasound-CT diagnostic correlation. **A**, Bimalleolar fracture: Heterogeneous hemarthrosis (arrow). **B**,**C**, Tibial plateau fracture with lipohemarthrosis and double fluid–fluid levels. Layers (superficial to deep): Fat (thin arrow), serous fluid (*), cellular debris (thick arrow). **C**, Hyperechoic fibrin strands (△) and fat-blood spheres (→). **D**, Axial CT: Lipohemarthrosis showing fat (thin arrow) and cellular layers (thick arrow). Indirect signs: subperiosteal hematoma, peri-fracture hematoma, subcutaneous soft-tissue.

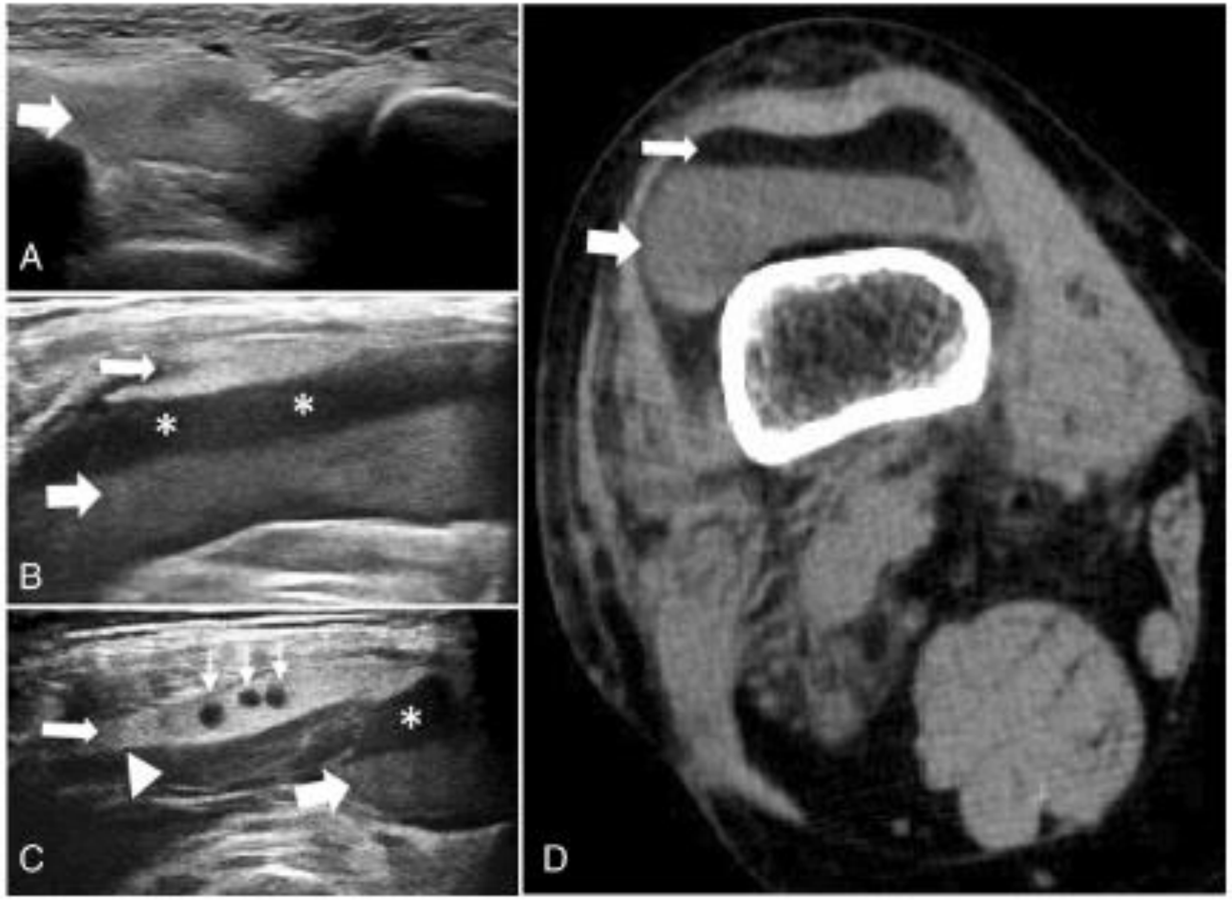

APR 2026 vol. 11 iss. 01 | POCUS J | 86

Intraocular Neoplasm Suggested by Ocular POCUS Examination

Felipe Hernández-Restrepo, MD*; Santiago Hernández-Moreno, MD; Alejandro Cardozo-Ocampo, MD

Emergency Department, Fundación Instituto Neurológico de Colombia, Medellín, Colombia

Abstract

We report the case of a 30-year-old woman with no relevant medical history who presented with a new-onset headache associated with nausea, vomiting, photophobia, phonophobia, and right nasal hemianopsia. Ocular point of care ultrasound (POCUS) examination revealed a hyperechoic lesion adhered to the vascular layer that did not move with eye movements. The patient was referred to ophthalmology, where choroidal melanoma was confirmed. Extension studies showed no metastases, and enucleation was performed. This case highlighted the importance of ocular POCUS in the diagnostic approach to this patient.

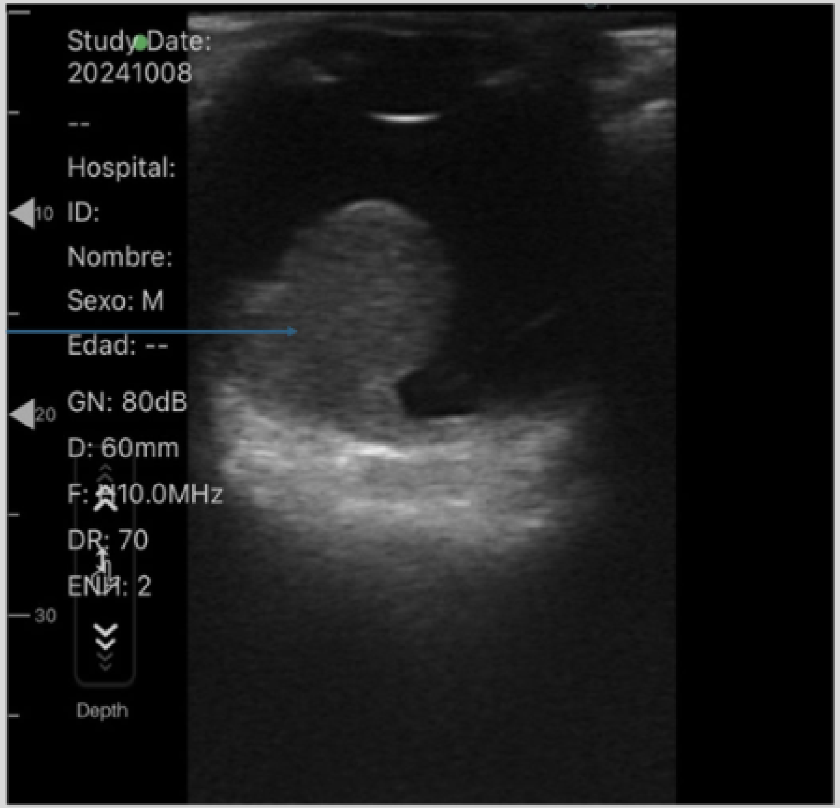

Figure 2. Ocular point of care ultrasound (POCUS) of the right eye The blue arrow points to a space-occupying lesion in the right globe.

Figure 3. Non-contrast head computed tomography scan. The blue arrow indicates a space-occupying lesion in the right globe.

Two-dimensional elastography and dispersion slope for allograft evaluation after pediatric liver transplantation

Jeong Min Song[1*], In Hye Song[2*], Hee Mang Yoon[1], Pyeong Hwa Kim[1], Ah Young Jung[1], Jin Seong Lee[1], Jung-Man Namgoong[3], Seak Hee Oh[4], Kyung Mo Kim[4], Young Ah Cho[1], Teresa Victoria[5]

[1]Department of Radiology and Research Institute of Radiology, [2]Department of Pathology, [3]Department of Pediatric Surgery, [4]Department of Pediatrics, Asan Medical Center, University of Ulsan College of Medicine, Seoul, Korea, [5]Department of Radiology, Massachusetts General Hospital, Boston, MA, USA

Purpose: This study evaluated the diagnostic performance of two-dimensional shear-wave elastography (2D SWE) for assessing allograft pathology in pediatric liver transplantation (LT) recipients, with subgroup analyses according to sonographic approach and age group. Additionally, the present study aimed to identify factors associated with SWE-derived parameters.

Methods: This study retrospectively analyzed pediatric LT recipients who had received a left lobe or left lateral segment graft during childhood and underwent paired 2D SWE and liver biopsy. Associations between elasticity and dispersion slope measurements and clinicopathologic parameters were evaluated using univariable and multivariable regression analyses. Subgroup analyses were performed according to sonographic approach and age group. Diagnostic performance was assessed using receiver operating characteristic analysis.

Results: A total of 108 patients (median age, 13.4 years; 47 males) were included. Elasticity measured using the intercostal approach in patients aged ≥13 years showed significant associations with METAVIR (Meta-analysis of Histological Data in Viral Hepatitis) fibrosis grade, necroinflammatory activity grade, liver allograft fibrosis score, and rejection activity index score. In multivariable analysis incorporating clinical parameters, METAVIR fibrosis grade remained the only independent predictor of intercostal elasticity in this age group (coefficient, 2.17; $P<0.001$). Intercostal elasticity demonstrated excellent diagnostic performance for distinguishing F0–F2 from F3–F4 fibrosis (area under the curve [AUC], 0.95; $P<0.001$; cut-off, 11.0 kPa) and good performance for distinguishing F0–F1 from F2–F4 fibrosis (AUC, 0.83; $P<0.001$; cut-off, 7.2 kPa). In contrast, subcostal measurements and dispersion slope showed no significant association with any pathologic parameter.

Conclusion: Intercostal elasticity demonstrated diagnostic value for predicting graft fibrosis in pediatric LT recipients aged ≥13 years who received left lobe or left lateral segment grafts. Among the evaluated clinicopathologic parameters, METAVIR fibrosis grade was the only independent predictor of elasticity in this subgroup.

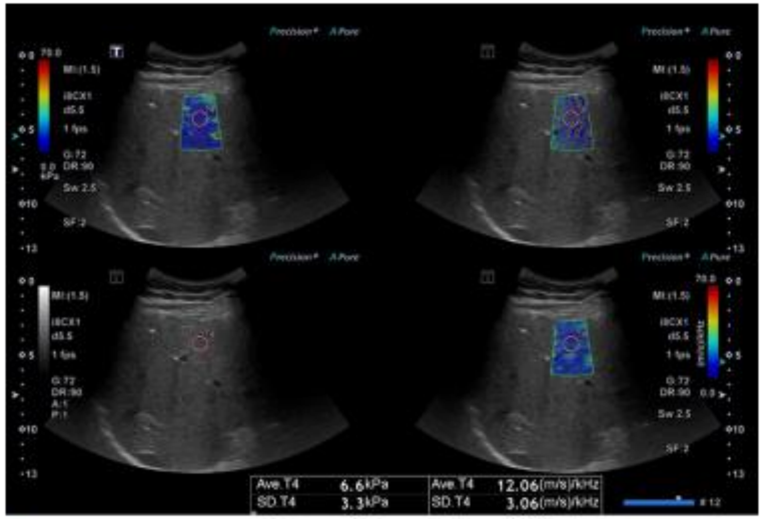

A

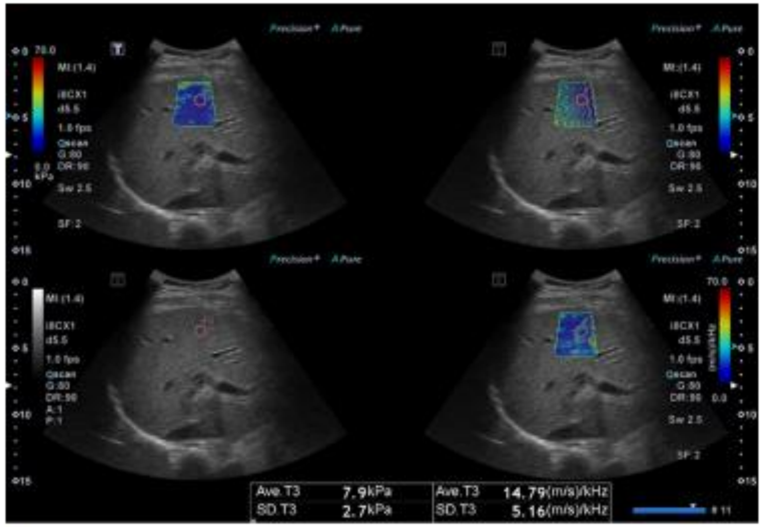

B

Fig. 2. Representative shear-wave elastography images obtained using the intercostal and subcostal approaches.

A. A 13-year-old girl with biliary atresia who underwent liver transplantation at 2 years of age and was evaluated as part of routine post-transplant surveillance presented. Two-dimensional shear-wave elastography demonstrated liver elasticity of 6.6 kPa and a dispersion slope of 11.9 (m/s)/kHz. Histopathologic examination demonstrated no fibrosis (METAVIR fibrosis grade F0), and all other pathologic findings were within normal limits (Intercostal scan). B. A 17-year-old girl with Wilson disease who underwent liver transplantation at 5 years of age and was evaluated because of suspected rejection presented. Two-dimensional shear-wave elastography demonstrated liver elasticity of 7.5 kPa and a dispersion slope of 13.1 (m/s)/kHz. Histopathologic examination demonstrated severe necroinflammatory activity (A3) with evidence of T-cell–mediated rejection, whereas no fibrosis was identified. In all examinations, measurements were obtained from liver parenchyma while avoiding vascular structures (subcostal scan).

APR 2026 vol. 11 iss. 01 | POCUS J | 96

Hepatocellular Carcinoma Masquerading as Heart Failure: When POCUS "Incidentally" Detects Cancer

Luke Shenton, MD MPH; Wesley Chow, MD; Bruce Kimura, MD*

Departments of Graduate Medical Education and Cardiology, Scripps Mercy Hospital, San Diego, CA, USA

Abstract

Hepatocellular carcinoma (HCC) is a leading cause of cancer-related death worldwide, and cardiovascular involvement can occur in advanced cases. An 84-year-old man with subacute dyspnea on exertion and pedal edema was referred to the cardiologist for suspected heart failure. Point of care ultrasound (POCUS) revealed scant ascites, a liver mass, and inferior vena cava (IVC) tumor thrombus extending into the right atrium. Computed tomography confirmed HCC with extensive intravascular spread and pulmonary emboli. This case illustrates a rare phenomenon of HCC masquerading as heart failure and underscores the potential value and challenges of incorporating POCUS into outpatient evaluations for earlier cancer detection.

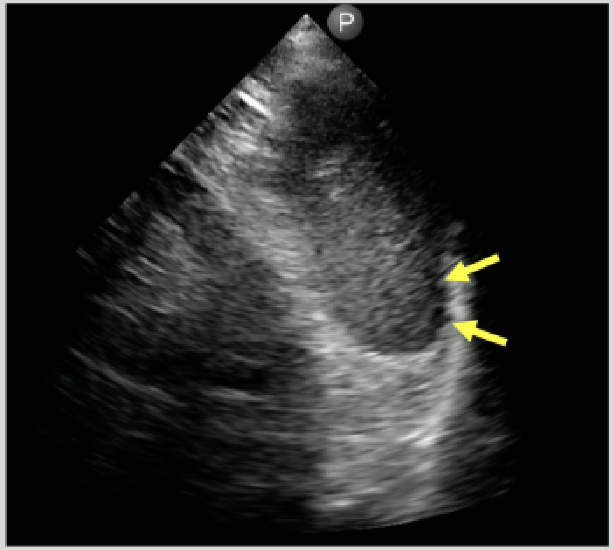

Figure 1. Mild ascites present when imaging the left lower thorax. A small amount of fluid is seen between the diaphragm and spleen (yellow arrows). [Philips Lumify 3.5 MHz cardiac transducer; right (cephalad direction)].

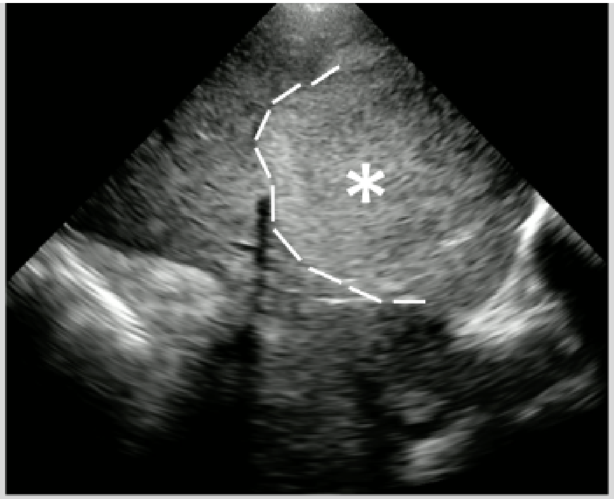

Figure 2. Evidence of a hyperechoic mass (*) in the liver, with notable absence of hepatic vessels. [Philips Lumify 3.5 MHz cardiac transducer; right (cephalad direction)].

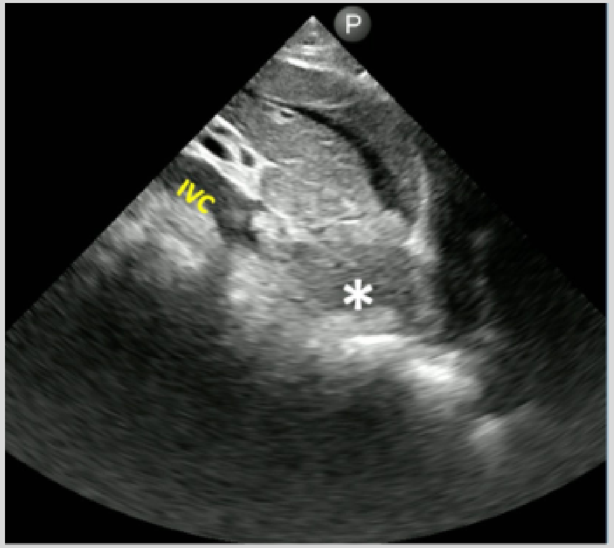

Figure 3. Inferior vena cave (IVC) appears occluded in the proximal portion by an infiltrating mass. [Philips Lumify 3.5 MHz cardiac transducer; right (cephalad direction)].

Quantitative ultrasound attenuation imaging outperforms B-mode scoring for assessing hepatic steatosis

Sadanobu Ogawa[1], Takashi Kumada[2,3], Tatsuya Gotoh[1], Fumihiko Niwa[1], Hidenori Toyoda[4], Tomoyuki Akita[3], Junko Tanaka[3], Masahito Shimizu[5]

[1]Department of Imaging Diagnosis, Ogaki Municipal Hospital, Ogaki; [2]Department of Nursing, Faculty of Nursing, Gifu Kyoritsu University, Ogaki; [3]Department of Epidemiology, Infectious Disease Control and Prevention, Hiroshima University Institute of Biomedical and Health Sciences, Hiroshima; [4]Department of Gastroenterology and Hepatology, Ogaki Municipal Hospital, Ogaki; [5]Department of Gastroenterology and Internal Medicine, Graduate School of Medicine, Gifu University, Gifu, Japan

Purpose: Accurate quantification of hepatic fat is essential for the management of metabolic dysfunction-associated steatotic liver disease; however, area under the receiver operating characteristic curve analysis is suboptimal for ordinal outcomes such as steatosis grade. This study compared the improved attenuation parameter (iATT) and the Hamaguchi score for hepatic steatosis assessment using the Obuchowski measure.

Methods: This prospective study enrolled 605 patients with chronic liver disease who underwent iATT measurement, Hamaguchi scoring, and magnetic resonance imaging–derived proton density fat fraction (MRI-PDFF) assessment between April 2021 and March 2024. iATT was measured using the ARIETTA 850 ultrasound system, whereas the Hamaguchi score was determined through blinded assessment of standardized images for hepatorenal contrast, liver brightness, deep attenuation, and vessel blurring. MRI-PDFF served as the reference standard, with thresholds defined as S0 (<5.2%), S1 (5.2% to <11.3%), S2 (11.3% to <17.1%), and S3 (≥17.1%). Diagnostic accuracy was evaluated using the Obuchowski measure, which weights pairwise comparisons across disease stages.

Results: Both methods showed strong correlations with MRI-PDFF (iATT: ρ=0.814; Hamaguchi score: ρ=0.799; P=0.533) and demonstrated excellent diagnostic performance. The Obuchowski measure was significantly higher for iATT than for the Hamaguchi score at S1 (0.921 vs. 0.875, P<0.001), S2 (0.931 vs. 0.892, P<0.001), and S3 (0.911 vs. 0.870, P<0.001). iATT performed significantly better in patients with body mass index (BMI) <30 kg/m^2, whereas the Hamaguchi score showed relatively better performance for detecting S1 steatosis in patients with obesity (BMI ≥30 kg/m^2).

Conclusion: The Obuchowski measure demonstrated that iATT provided significantly better ordinal discriminatory performance than the Hamaguchi score for the assessment of hepatic steatosis.

Keywords: Ultrasonography; Magnetic resonance imaging; Fatty liver; Body mass index; Obesity

Key points: Quantitative ultrasound using improved attenuation parameter (iATT) showed higher ordinal discriminatory performance than the Hamaguchi score when evaluated using the Obuchowski measure. iATT performed better in patients without obesity and in those with shorter skin-to-capsule distance, whereas the Hamaguchi score performed relatively better in patients with obesity and greater skin-to-capsule distance. The Obuchowski measure enabled appropriate evaluation of diagnostic tests with ordinal classifications beyond conventional area under the receiver operating characteristic curve analysis.

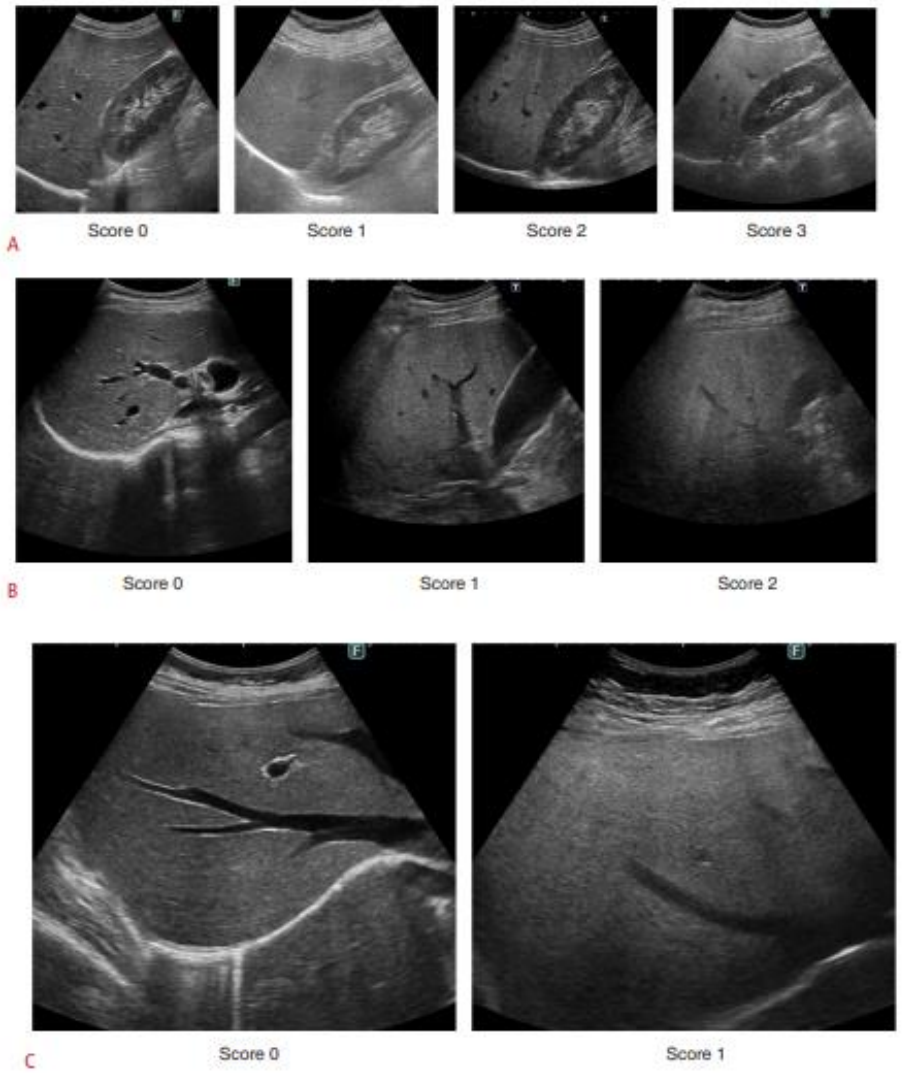

Fig. 2. **Hamaguchi score components.**
Representative ultrasound images shows the three components of the Hamaguchi scoring system obtained using standardized ARIETTA 850 settings. A. Hepatorenal contrast and liver brightness: scores of 0–3 were assigned according to echogenicity relative to the renal cortex and visibility of intrahepatic structures. B. Deep-beam attenuation: scores of 0–2 were assigned according to posterior liver visualization and diaphragmatic clarity. C. Vessel blurring: scores of 0–1 were assigned according to the definition of intrahepatic vessel borders and wall clarity.

Quantitative ultrasound attenuation imaging outperforms B-mode scoring for assessing hepatic steatosis

Sadanobu Ogawa[1], Takashi Kumada[2,3], Tatsuya Gotoh[1], Fumihiko Niwa[1], Hidenori Toyoda[4], Tomoyuki Akita[3], Junko Tanaka[3], Masahito Shimizu[5]

[1]Department of Imaging Diagnosis, Ogaki Municipal Hospital, Ogaki; [2]Department of Nursing, Faculty of Nursing, Gifu Kyoritsu University, Ogaki; [3]Department of Epidemiology, Infectious Disease Control and Prevention, Hiroshima University Institute of Biomedical and Health Sciences, Hiroshima; [4]Department of Gastroenterology and Hepatology, Ogaki Municipal Hospital, Ogaki; [5]Department of Gastroenterology and Internal Medicine, Graduate School of Medicine, Gifu University, Gifu, Japan

Purpose: Accurate quantification of hepatic fat is essential for the management of metabolic dysfunction-associated steatotic liver disease; however, area under the receiver operating characteristic curve analysis is suboptimal for ordinal outcomes such as steatosis grade. This study compared the improved attenuation parameter (iATT) and the Hamaguchi score for hepatic steatosis assessment using the Obuchowski measure.

Methods: This prospective study enrolled 605 patients with chronic liver disease who underwent iATT measurement, Hamaguchi scoring, and magnetic resonance imaging–derived proton density fat fraction (MRI-PDFF) assessment between April 2021 and March 2024. iATT was measured using the ARIETTA 850 ultrasound system, whereas the Hamaguchi score was determined through blinded assessment of standardized images for hepatorenal contrast, liver brightness, deep attenuation, and vessel blurring. MRI-PDFF served as the reference standard, with thresholds defined as S0 (<5.2%), S1 (5.2% to <11.3%), S2 (11.3% to <17.1%), and S3 (≥17.1%). Diagnostic accuracy was evaluated using the Obuchowski measure, which weights pairwise comparisons across disease stages.

Results: Both methods showed strong correlations with MRI-PDFF (iATT: ρ=0.814; Hamaguchi score: ρ=0.799; P=0.533) and demonstrated excellent diagnostic performance. The Obuchowski measure was significantly higher for iATT than for the Hamaguchi score at S1 (0.921 vs. 0.875, P<0.001), S2 (0.931 vs. 0.892, P<0.001), and S3 (0.911 vs. 0.870, P<0.001). iATT performed significantly better in patients with body mass index (BMI) <30 kg/m^2, whereas the Hamaguchi score showed relatively better performance for detecting S1 steatosis in patients with obesity (BMI ≥30 kg/m^2).

Conclusion: The Obuchowski measure demonstrated that iATT provided significantly better ordinal discriminatory performance than the Hamaguchi score for the assessment of hepatic steatosis.

Tính toán thước đo Obuchowski

Chỉ số Obuchowski cung cấp đánh giá toàn diện về độ chính xác chẩn đoán đối với các kết quả thứ tự bằng cách kết hợp tất cả các so sánh từng cặp có thể có giữa các loại bệnh [10–12Ma trận trọng số gán các trọng số khác nhau tùy thuộc vào ý nghĩa lâm sàng của việc phân loại sai. So sánh giữa các cấp độ liền kề (S0 so với S1) được gán trọng số là 0,5, so sánh giữa các cấp độ cách nhau hai giai đoạn (S0 so với S2) được gán trọng số là 0,75, và so sánh giữa các cấp độ cách nhau ba giai đoạn (S0 so với S3) được gán trọng số là 1,0.
Đối với mỗi cặp bệnh nhân có mức độ gan nhiễm mỡ thực sự khác nhau, hiệu quả chẩn đoán được đánh giá dựa trên việc xét nghiệm có xếp hạng chính xác cặp bệnh nhân đó hay không. Điểm số 1, 0,5 và 0 được gán tương ứng cho việc xếp hạng chính xác, giá trị bằng nhau và xếp hạng không chính xác. Chỉ số Obuchowski được tính bằng tổng có trọng số của tỷ lệ các cặp được xếp hạng chính xác trên tất cả các so sánh mức độ gan nhiễm mỡ.

Trong phép tính này, w_{ij} là trọng số được gán cho sự so sánh giữa điểm i và j, và P_{ij} là tỷ lệ các cặp được sắp xếp chính xác. Khoảng tin cậy (CI) được xây dựng bằng cách sử dụng phương pháp lấy mẫu lại bootstrap theo phần trăm với 2.000 lần lặp. Sự khác biệt giữa iATT và điểm Hamaguchi được kiểm tra bằng cách sử dụng các mẫu bootstrap ghép cặp.

Hamaguchi score protocol

B-mode ultrasonographic evaluation was performed immediately before iATT measurement using the same ultrasound system [3]. Hepatic steatosis was graded using the Hamaguchi scoring system, which consists of three components: (1) hepatorenal contrast/liver brightness (0–3 points: 0 = normal echogenicity; 1 = mild increase with preserved visualization of intrahepatic structures; 2 = moderate increase with slight impairment of visualization; and 3 = marked increase with poor visualization), (2) deep attenuation (0–2 points: 0 = none; 1 = mild attenuation with distinguishable structures; and 2 = marked attenuation with signal loss), and (3) vessel blurring (0–1 point: 0 = sharp vessel margins and 1 = blurred vessel margins), yielding a total score ranging from 0 to 6 points (Fig. 2) [8].

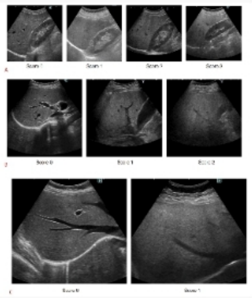

Hình 2.

Các thành phần của thang điểm Hamaguchi.

Hình ảnh siêu âm tiêu biểu cho thấy ba thành phần của hệ thống chấm điểm Hamaguchi thu được bằng cách sử dụng cài đặt tiêu chuẩn ARIETTA 850. **A.** Độ tương phản gan thận và độ sáng của gan: điểm số từ 0–3 được gán dựa trên độ phản âm so với vỏ thận và khả năng hiển thị các cấu trúc trong gan. **B.** Độ suy giảm chùm tia sâu: điểm số từ 0–2 được gán dựa trên khả năng hiển thị phần sau của gan và độ rõ nét của cơ hoành. **C.** Độ mờ của mạch máu: điểm số từ 0–1 được gán dựa trên độ rõ nét của ranh giới mạch máu trong gan và độ rõ nét của thành mạch.

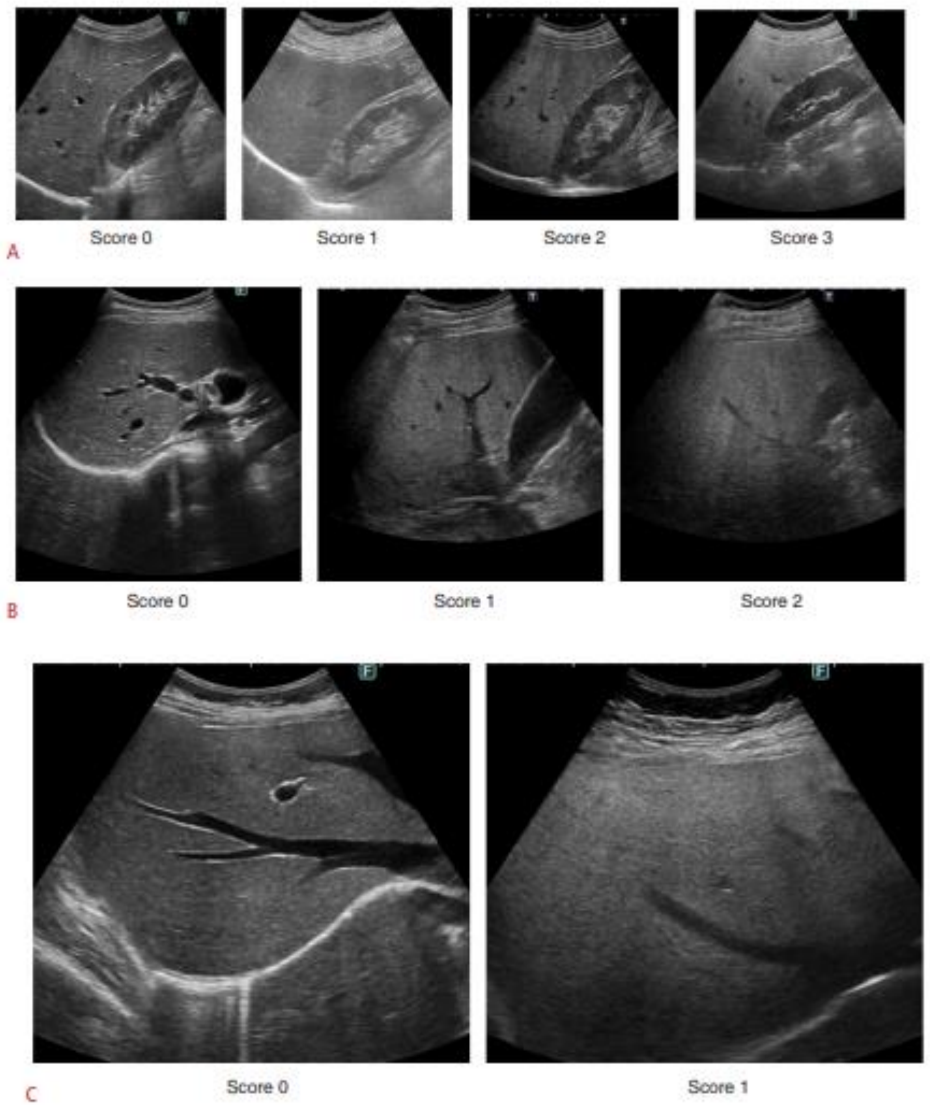

Fig. 2. Hamaguchi score components.
Representative ultrasound images shows the three components of the Hamaguchi scoring system obtained using standardized ARIETTA 850 settings. A. Hepatorenal contrast and liver brightness: scores of 0–3 were assigned according to echogenicity relative to the renal cortex and visibility of intrahepatic structures. B. Deep-beam attenuation: scores of 0–2 were assigned according to posterior liver visualization and diaphragmatic clarity. C. Vessel blurring: scores of 0–1 were assigned according to the definition of intrahepatic vessel borders and wall clarity.

Hình 2.
Các thành phần của thang điểm Hamaguchi.
Hình ảnh siêu âm tiêu biểu cho thấy ba thành phần của hệ thống chấm điểm Hamaguchi thu được bằng cách sử dụng cài đặt tiêu chuẩn ARIETTA 850. **A.** Độ tương phản gan thận và độ sáng của gan: điểm số từ 0–3 được gán dựa trên độ phản âm so với vỏ thận và khả năng hiển thị các cấu trúc trong gan. **B.** Độ suy giảm chùm tia sâu: điểm số từ 0–2 được gán dựa trên khả năng hiển thị phần sau của gan và độ rõ nét của cơ hoành. **C.** Độ mờ của mạch máu: điểm số từ 0–1 được gán dựa trên độ rõ nét của ranh giới mạch máu trong gan và độ rõ nét của thành mạch.

www.nature.com/scientificreports

scientific reports

OPEN

Fat mass index as a screening tool for the assessment of non-alcoholic fatty liver disease

Shengkui Zhang[1,2], Lihua Wang[1], Miao Yu[1], Weijun Guan[1] & Juxiang Yuan[1]

Non-alcoholic fatty liver disease (NAFLD) is replacing hepatitis B as the leading cause of chronic liver disease in China. The purpose of this study is to select good tools to identify NAFLD from the body composition, anthropometry and related routine clinical parameters. A total of 5076 steelworkers, aged 22–60 years, was included in this study. Body fat mass was measured via bioelectrical impedance analysis (BIA) and fat mass index (FMI) was derived. Ultrasonography method was used to detect hepatic steatosis. Random forest classifier and best subset regression were used to select useful parameters or models that can accurately identify NAFLD. Receiver operating characteristic (ROC) curves were used to describe and compare the performance of different diagnostic indicators and algorithms including fatty liver index (FLI) and hepatic steatosis index (HSI) in NAFLD screening. ROC analysis indicated that FMI can be used with high accuracy to identify heavy steatosis as determined by ultrasonography in male workers [area under the curve (AUC) 0.95, 95% CI 0.93–0.98, sensitivity 89.0%, specificity 91.4%]. The ability of single FMI to identify NAFLD is no less than that of combination panels, even better than the combination panel of HSI. The best subset regression model that including FMI, waist circumference, and serum levels of triglyceride and alanine aminotransferase has moderate accuracy in diagnosing overall NAFLD (AUC 0.83). FMI and the NAFLD best subset (BIC) score seem to be good tools to identify NAFLD in Chinese steelworkers.

Assessment of NAFLD. The diagnosis of NAFLD have been described in detail in one of our previous studies[19]. In brief, ultrasonography method was used to detect hepatic steatosis[21]. Subsequently, according to the ultrasound imaging criteria[22], the fatty liver was divided into three grades: grade 1 (light), grade 2 (moderate), and grade 3 (heavy). The final assessment of NAFLD excluded secondary hepatic steatosis, including excess alcohol intake (over 140 g/week for men and 70 g/week for women), hepatitis B infection, hepatitis C infection, autoimmune, celiac disease, genetic disorders such as Wilson's disease, alpha-1-antitrypsin deficiency liver diseases, hepatic malignancies, hepatobiliary infections, biliary tract, and related medications (tamoxifen, amiodarone, methotrexate, glucocorticoids) based on the above ultrasonography results[23,24].

Anthropometric measurements. The values of fat mass and BF% were measured by the Body Composition Analyzer (TANITA BC-420, Japan). The manufacturer's protocols[18] and the intra-rater reliability[20] of the body composition analyzer of the same brand and model have been described in detail elsewhere. The measurement criteria of height, weight, waist circumference and hip circumference (HC) in this study were shown in our previous study[20]. The detailed definitions of BF%, FMI, BMI, waist-to-hip ratio (WHR) and waist-to-height ratio (WHtR) have been elaborated in our previous study[20]. Blood pressure measurements were performed three times five-minute intervals using an electronic sphygmomanometer (OMRON, HBP-1100, China), and the participants were required to rest for more than ten minutes. Finally, the mean was obtained for analysis.

Measurement of laboratory parameters. Overnight fasting blood samples were drawn for determination of fasting plasma glucose (FPG), total cholesterol (TC), triglycerides (TG), low-density lipoprotein (LDL-C), high-density lipoprotein (HDL-C), alanine aminotransferase (ALT), aminotransferase (AST), γ-glutamyl transferase (GGT), platelet count (PLT), serum uric acid, and albumin. All blood samples were tested in the central laboratory of Tangshan Hongci Hospital Laboratory using automatic biochemical analysers (mindrary, BS-800, China) within four hours.

Phân biệt GNM do rượu và không do rượu

Gần như không có sự khác biệt nào trên hình ảnh siêu âm giữa gan nhiễm mỡ do rượu và gan nhiễm mỡ liên quan đến rối loạn chuyển hóa (MASLD - trước đây gọi là NAFLD).

Sự khác biệt trên siêu âm chỉ có thể xuất hiện mang tính chất gợi ý khi bệnh đã tiến triển đến giai đoạn **xơ gan (Cirrhosis)**:

Xơ gan do rượu: Thường có xu hướng tạo ra xơ gan hạt nhỏ (micronodular), bề mặt gan có thể gồ ghề nhẹ nhưng tương đối đều. Gan có thể teo lại hoặc đôi khi vẫn to do viêm gan rượu đi kèm.
Xơ gan do MASLD: Thường tạo ra xơ gan hạt to (macronodular) ở giai đoạn muộn, bề mặt gan có thể có các nốt không đều rõ rệt hơn.
Tuy nhiên, những dấu hiệu này không đặc hiệu và không thể dùng làm tiêu chuẩn vàng để chẩn đoán nguyên nhân.

Vì hình ảnh siêu âm là như nhau, việc phân biệt bắt buộc phải dựa vào **lâm sàng và xét nghiệm máu**:

- **Lịch sử tiêu thụ cồn (Yếu tố quyết định):**
  - **Do rượu:** Bệnh nhân nam uống > 30g cồn/ngày, hoặc nữ > 20g cồn/ngày trong thời gian dài.
  - **MASLD:** Bệnh nhân uống rất ít hoặc không uống rượu (dưới ngưỡng trên), nhưng có kèm theo ít nhất một yếu tố của hội chứng chuyển hóa (thừa cân/béo phì, tiểu đường type 2, cao huyết áp, rối loạn mỡ máu).
- **Xét nghiệm máu (Men gan):**
  - **Do rượu:** Chỉ số AST thường tăng cao hơn ALT. Tỷ lệ AST/ALT thường lớn hơn 2 (đôi khi >3). Chỉ số GGT (Gamma-GT) cũng thường tăng rất cao.
  - **MASLD:** Chỉ số ALT thường tăng cao hơn AST. Tỷ lệ AST/ALT thường nhỏ hơn 1 (cho đến khi bệnh tiến triển thành xơ gan thì tỷ lệ này mới đảo ngược).
- **Thể tích hồng cầu (MCV):** Bệnh nhân gan do rượu thường có hồng cầu to (MCV tăng), trong khi MASLD thường có MCV bình thường.

JOURNAL OF
MEDICAL ULTRASOUND

MENU

Search

< Previous Next >

REVIEW ARTICLE

Evaluating the Role of Ultrasonography in Diagnosing Alcohol-associated Liver Disease in Low-resource Settings: A Critical Review of Current Evidence

Challa, Maheswara Rao[1,*]; Gnanavel, A.[2]; Theja, E. Ravi[3]; Kesavi, D.[3]; Kumar, S. Saravana[2]

Author Information

Journal of Medical Ultrasound 34(2):p 148-154, Apr–Jun 2026.
| DOI: 10.4103/jmu.JMU-D-25-00079

Table 4: Integrated diagnostic algorithm for alcohol-associated liver disease in low-resource settings[1,14]

Step	Tools/markers used	Purpose
Initial screening	Alcohol use history, AST/ALT, platelet count	Identify at-risk individuals
Sonographic evaluation	Hepatic echotexture, splenic size	Detect structural liver changes
Noninvasive fibrosis score	APRI, FIB-4	Assess fibrosis severity
Advanced imaging referral	Elastography/CT (if available)	Confirm staging in ambiguous cases

AST: Aspartate aminotransferase, ALT: Alanine aminotransferase, CT: Computed tomography, APRI: AST-to-platelet ratio index, FIB-4: Fibrosis-4

Table 4: Integrated diagnostic algorithm for alcohol-associated liver disease in low-resource settings[1,14]

Step	Tools/markers used	Purpose
Initial screening	Alcohol use history, AST/ALT, platelet count	Identify at-risk individuals
Sonographic evaluation	Hepatic echotexture, splenic size	Detect structural liver changes
Noninvasive fibrosis score	APRI, FIB-4	Assess fibrosis severity
Advanced imaging referral	Elastography/CT (if available)	Confirm staging in ambiguous cases

AST: Aspartate aminotransferase, ALT: Alanine aminotransferase, CT: Computed tomography, APRI: AST-to-platelet ratio index, FIB-4: Fibrosis-4

SIÊU ÂM ĐỊNH LƯỢNG MASLD

Hai thông số quan trọng nhất hiện nay để đánh giá toàn diện một ca MASLD (gan nhiễm mỡ không do rượu) bao gồm: **Định lượng mỡ (CAP/ATI)** và **Định lượng xơ hóa (Độ cứng - Stiffness)**.

Bảng phân độ nhiễm mỡ định lượng (Giá trị tham chiếu CAP)

Đơn vị đo là decibel trên mét (dB/m). Chỉ số này càng cao, gan nhiễm mỡ càng nặng:

Chỉ số CAP (dB/m)	Tương đương độ nhiễm mỡ	Tỷ lệ tế bào gan tích mỡ
< 248	**S0:** Bình thường	Dưới 5%
248 – 268	**S1:** Nhiễm mỡ Nhẹ	5% – 33%
268 – 280	**S2:** Nhiễm mỡ Vừa	34% – 66%
> 280	**S3:** Nhiễm mỡ Nặng	Trên 66%

Bảng phân độ xơ hóa gan (Metavir Score)

Dưới đây là bảng điểm chuẩn để đánh giá giai đoạn xơ hóa ở bệnh nhân MASLD (Lưu ý: trị số cắt kPa có thể thay đổi nhẹ tùy theo dòng máy FibroScan hay 2D-SWE của các hãng):

Độ cứng gan (kPa)	Vận tốc (m/s)	Phân độ Metavir	Ý nghĩa lâm sàng
< 6.0	< 1.4	**F0 / F1**	Không xơ hóa hoặc xơ hóa nhẹ quanh mạch máu.
6.0 – 8.0	1.4 – 1.6	**F2**	Xơ hóa có ý nghĩa (bắt đầu hình thành các dải xơ lan ra ngoài).
8.0 – 12.0	1.6 – 2.0	**F3**	Xơ hóa nặng (các dải xơ nối với nhau thành cầu nối cấu trúc).
> 12.0	> 2.0	**F4**	**Xơ gan** (cấu trúc gan bị đảo lộn hoàn toàn).

3. Bản đồ màu định lượng (B-mode kết hợp Màu)

Trên các dòng máy siêu âm hiện đại, tính năng định lượng không chỉ cho ra một con số mà còn hiển thị dưới dạng **Bản đồ màu (Color Map)** đè lên hình ảnh 2D:

- **Với đo mỡ (ATI):** Vùng nào có hệ số giảm âm đồng đều sẽ hiện màu xanh lục ổn định, giúp bác sĩ tránh chọn vào các mạch máu lớn hay bóng cản của sườn, đảm bảo kết quả đo chính xác nhất.
- **Với đo xơ hóa (Elastography):** Máy hiển thị một thang màu từ xanh dương (mô mềm) đến đỏ/vàng (mô cứng). Nếu vùng gan nhiễm mỡ đã chuyển sang viêm hoặc xơ, bản đồ màu sẽ lốm đốm các mảng màu ấm (vàng/đỏ) thể hiện mô gan đang bị mất độ đàn hồi.

Ưu điểm vượt trội: Sự kết hợp giữa siêu âm B-mode, đo mỡ (dB/m) và đo độ cứng (kPa) trong cùng một lần khám giúp bệnh nhân MASLD theo dõi chính xác phác đồ điều trị (chế độ ăn, tập luyện, thuốc) xem lượng mỡ có giảm đi hay độ cứng của gan có được cải thiện theo thời gian hay không – điều mà siêu âm mắt thường không bao giờ làm được.